University of Leiden **Faculteit der Wiskunde en Natuurwetenschappen** *20th August 2012*
Leiden **Bachelor**

Real-time oxidation monitoring of a cavity aperture using reflection

BACHELOR THESIS BY: **Henk Snijders**

Research Group: Quantum Optics

Group Leader: Prof. Dr. D. Bouwmeester

Supervisor: Dr. M.P. van Exter

Supervisor: MSc M.P. Bakker

Supervisor: MSc D.T. Suntrup

Period: february 2012 - August 2012

Contents

Chapter 1

Introduction

In this Bachelor thesis, I will show the control of the oxidation of an oxide aperture using a change in the reflection spectrum of the micropillar. An aperture of the right size will improve the confinement of the light into an optical microcavity.

Microcavities

Nowadays, fields as quantum information and quantum electrodynamics are interesting fields of research for the implementation of a quantum computer. The main goal is to implement solid sate storage qubits through electron spins, while data transfer and manipulation are done by photons that are entangled with the qubits. To do this, we work with quantum dots[1] in optical micropillars[2]. Quantum dots confine excitons in an 3D potential. The micropillar is used to enhance the coupling of the light within the quantum dot. This way the quantum dot has a stronger coupling with an external optical mode. To quantify the coupling of an external optical mode we use the Purcell factor. This factor is the ratio of emission rate of an atom in a cavity relative to that of an atom in the free space. The Purcell factor is proportional to Q/V, where Q is the quality factor defined as the wavelength of the resonance divided by the full width at half maximum, and V the effective mode volume in the cavity. In the field of cavity quantum electro dynamics(CQED) various types of microcavities are being investigated besides micropillars[3]. Microtoroids[4],they can have an ultrahigh-Q but have typically a fairly large mode volume. Photonic crystal membrane cavities [5][6]can have a very small mode volume V but are usually polarization non degenerate. We work not with free-standing micropillar structures but with remaining DBR-structures surrounding the pillars. This is done so that the quantum dot can be controlled using electrical gates and these can control the electron charging of the quantum dots. Using the Stark shift, the quantum dot can be tuned in resonance by an external optical mode. The use of this outweighs the fact that these cavity structures do not have the highest Q. Also these micropillars are easy to be made polarization degenerate.

Oxidation process

For the oxidation there is reaction between aluminium and the oxygen atom. The oxygen atom is provided in the form of water, which is called wet oxidation. According to [7] there

are two chemical reactions that happen.

$$2AlAs + 3H_2O_{(g)} \rightarrow Al_2O_3 + 2AsH_3 \tag{1.1}$$

$$2AlAs + 4H_2O_{(g)} \rightarrow 2AlO(OH) + 2AsH_3 \tag{1.2}$$
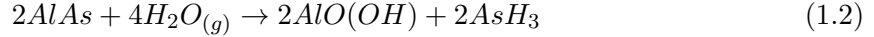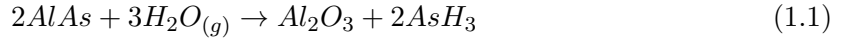
Reaction 1.1 mainly happens, although if the reaction conditions change, the other reaction can be favored. In [7] it said that at the end of a thin oxidation taper reaction 1.2 is mainly happening, which gives a more porous structure than reaction 1.1. Due to the oxidation of $AlAs$ to Al_2O_3 the refractive index will change from 3.0 to 1.8 and this results in transverse plane confinement of light into the cavity.

For our reactions we mainly use H_2O which diffuses more easily into the sample, because it has half the size of an O_2 molecule. In general the oxidation is dependent on the following factors: time, oxidation temperature[8], thickness of the oxidation layer, the aluminium concentration in the layer and the structure to be oxidized. Only the time and temperature can be changed in our setup. A higher aluminium concentration will result in a higher oxidation rate. The oxidation taper in the sample has a maximum aluminium concentration. The DBR-mirrors around the sample also contain some layers with less aluminium. So that the oxidation goes more slowly. The growth of the oxide aperture depends on the crystal lattice structure of AlAs. Due to the lattice structure there is a fast and a slow oxidation axis. This is why an elliptical micropillar can give a round aperture and vice versa. The oxidation process of AlAs normally takes place in an oxidation oven at $400\,^\circ$C for about 40 minutes. With these conditions the oxidation rate is typically about 0.25 μm per minute. The samples are made in wafers, and from a piece of a wafer 12 samples are made. For each wafer the oxidation temperature and oxidation time of the oven need to be calibrated again, because there are fluctuations in the thickness of the AlAs layer in each wafer. It is assumed that at a piece of wafer from which 12 samples are made, the thickness of the AlAs layer is constant. Most of the 12 samples will be used to calibrate the oven and then maybe two samples will have a cavity with a good aperture which results in a cavity with a high Q-factor. To control the oxidation such that a small cavity is produced is really hard because the circular structures we use will have an increased oxidation speed if the aperture becomes very small[9]. This oxidation speed will increase because the oxidation fronts start to overlap each other. Still our goal is to monitor the oxidation real-time.

Measurement techniques
We tried two measurement techniques to control the oxidation:

- monitoring the cavity modes using a 'resonant broadband' reflection technique,

- Monitoring changes in the side lobes of the reflection spectrum of a cavity at a wavelength of 1064nm.

The first method of measuring the cavity modes with reflection or photoluminescence did not work, because the cavity modes vanished at higher temperatures due to absorption of the frequency-shifted bandgap. So reading the paper of Almuneau et al.[10] gave us the idea to measure the change in the side lobes of a cavity reflection spectrum as result of a change in the refractive index due to the oxidation. This method was applied with success.

Chapter 2

Setup/Experimental details

2.1   Optical setup

A schematic drawing of the experimental setup is given in Fig. 2.1. It consists of two parts: an optical setup and the oven in which the sample is placed.

Spectrometer
The spectrometer used is a Hilgert Engis Monospec 1000 equipped with an Andor IDus DU401A-BR-DD. It has a resolution of 19 nm/1024 pixels, that is 0.019 nm per pixel. Furthermore it is important to know that the spectrometer is polarization dependant due to the grating within the spectrometer, because the gratings have a polarization dependant diffraction efficiency. So to change the polarization, the setup includes a $\lambda/2$ waveplate. This is done to get a smoother reflection spectrum at the position of the DBR and cavitymodes.

Objective
In the setup a Mitutoyo Plan Apo NIR Infinity-Corrected Objective NT46-404 is used with a focal length of 10 mm, NA of 0.40, a magnification of $20\times$ and a working distance of 20 mm.

Lightsource
For PL-measurements a L780P010 Thorlabs laser diode with a wavelength of 780 nm and an output power of 3 mW is used. At the sample we measured a laser power of 0.8 mW. The light is coupled to the spectrometer with a multi-mode fiber, because the higher order modes are then better visible. all the multi-mode fibers in our experiment have a core size of 62.5 μm and a cladding diameter of 125 μm. A Super Luminescent Emitting Diode(SLED) from Superlum Ireland (SLD-47-HP) is placed in the setup to measure the DBR and the cavity modes through reflection. The output power is 10 mW and the wavelength range goes from 880 to 1000 nm. In this case the light is single-mode coupled to the spectrometer because then we have a better mode-matching and the noise of the signal decreases. This way the modes are more visible, however some intensity of the higher order modes is lost. The SLED in the optical setup is very sensitive to optical feedback. This is light which is reflected from the sample back into SLED, where it interferes with the outcoming signal. Because of this our signal on the spectrometer gives instabilities and power spikes. For this reason an optical isolator is used. For the side lobes of the DBR-cavity reflection spectrum a Laser from CrystaLaser (IRCL-
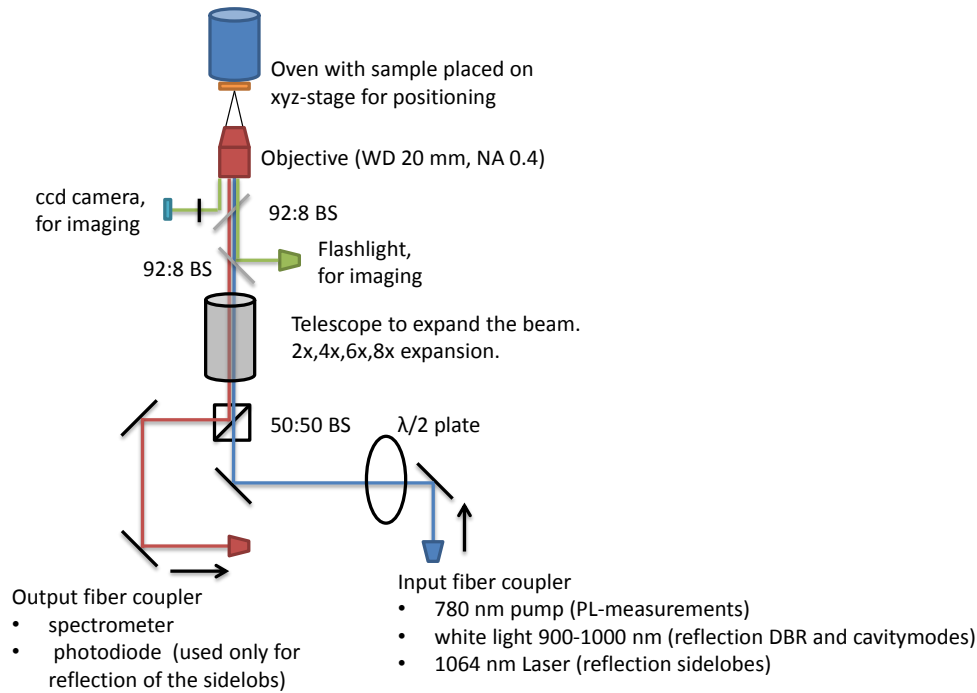
Figure 2.1: *The experimental setup. In both fiber couplers an aspherical lens with f=18,4 mm and NA=0.15 is used. The telescope is included to get effectively a smaller spot on the sample*

100-1064s) with a wavelength of 1064 nm and an output power of 100 mW is used. The signal is collected with a single mode fiber and then coupled to a fiber-coupled photodiode. The photodiode is a PDA100A-Ec Thor-Labs Si-detector with a wavelength range of 400-1100 nm.

Telescope
A telescope was placed in the setup to couple the light better into the cavity. This way the higher order modes are more visible. The telescope will increase the size of the collimated beam to better fill the objective. Now a smaller spot is possible due to the diffraction limited spot size.

2.2   Oxidation oven

The first idea was to use an oven placed on a hot plate but this gave a couple of problems. There were many problems to get the window of the oven to 100 °C, because of the low conductance of the glass the rest of the oven had to heat up to 200 °C. The result was that

the O-rings could not withstand a temperature of 200 °C. If the O-rings are burned HF can come free, which is lethal in high concentrations. Another problem was the drift of the sample in the oven. The hot plate has a large thermal expansion, so the hot plate ensured that the sample was raised a few millimeters. As seen in the picture of the oven below, the oven is also quite big so there is a lot of energy needed to heat up the oven to a bit more than 100 °C. Below a picture of our old oven in Fig.2.2.


Figure 2.2: *Picture of the old oven. The fact that a lot of energy was needed to heat up the oven, combined with the large thermal drift made us decide to build a new oven.*

Below in Fig.2.3 and Fig.2.4 you see the new oven built at the Fijn Mechanische Dienst Leiden institute of Physics. This much smaller oven is 10 cm long, has a radius of 4 cm, and is made from stainless steel. The central rod is made from copper to provide a good heat conductance between the firerod and the sample. The central firerod is a Omega CSH-101100 of 100 W which can go to a maximum temperature of 450 °C. At higher temperatures the wires will burn. The 6 firerods of type omega CSM-1011001 in the outside of the oven have a output power of 100 W and can go to a temperature of 250 °C. The firerods are represented in red in the cross-section in Fig.2.3. There is a sapphire instead of a glass window placed in this oven, because sapphire has a much higher thermal conductivity. To place the window in the outside of the oven we use a Bison Mastic Silicone kit which can go to temperatures of 250 °C and for a short period of one hour even to 300 °C. The input steam comes from a water bubbler on a hotplate and then goes through a three way valve. One way is connected to the oven, while the other is connected to a tube so that we can check if the steam flow is alright.
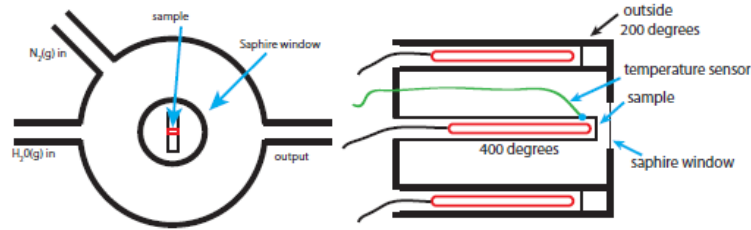
Figure 2.3: *Schematic pictures of the oven. The left one is the frontside of the oven and the right one is a cross-section. The central pillar of the oven is heated up to 400°C while the outside is heated up to 200°C to prevent the steam from condensing on the mirror.*

The steam which comes out of the oven goes through a condenser and the remaining gas is then sucked up into the airdrain. This is done because during the oxidation process some arsenide can come free[11]. There is also a N_2 input in the oven to stop the oxidation by blowing out the steam and it is also used to cool the oven down. Stopping the oxidation by blowing out the water this way didn't seem to work very well so the N_2 was mainly used to cool the sample down. The outside of the oven was cooled down using two Paps ventilators. Using the ventilators it took about 40 minutes to cool the sample down from 420 °C to 30 °C. The temperature of the oven itself is controlled using a Hemi Heating HTC-4400 temperature controller. The temperature of the copper rod, on which the sample is mounted, is controlled with a Euroterm 3216 temperature controller. To make sure that the objective does not heat up, which has a distance smaller than 2 cm from the window, a polished aluminium shield is used. The oven is placed on a xyz-translation stage with computer controlled actuators. A Newport ESP 301 Motion controller is used with 3 LTA-HL-S/n-B0408-75173-2483 actuators with a resolution of 7.37 nm and a backslash of 6.0 μm ,7.2 μm,7.2 μm respectively. The tubes connected to the oven are flexible so we can do a spatial scan by moving the entire oven.
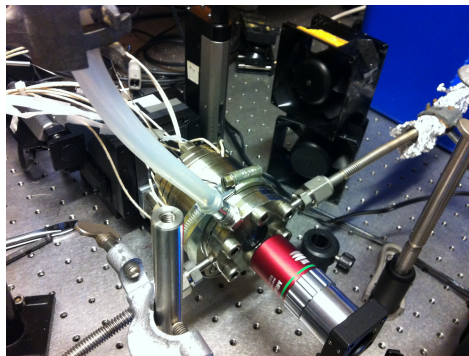
Figure 2.4: *Here is a picture of the final oven. The heat shield is removed for visibility.*

2.3   Sample description

Below you see in Fig.2.5 our micropillar sample. The sample contains 6×7 cavities and a marker. The micropillar has a diameter of about 30 μm and has three connections called 'bridges' for electrical contacts. The three trenches of the cavities each go down to the bottom DBR.
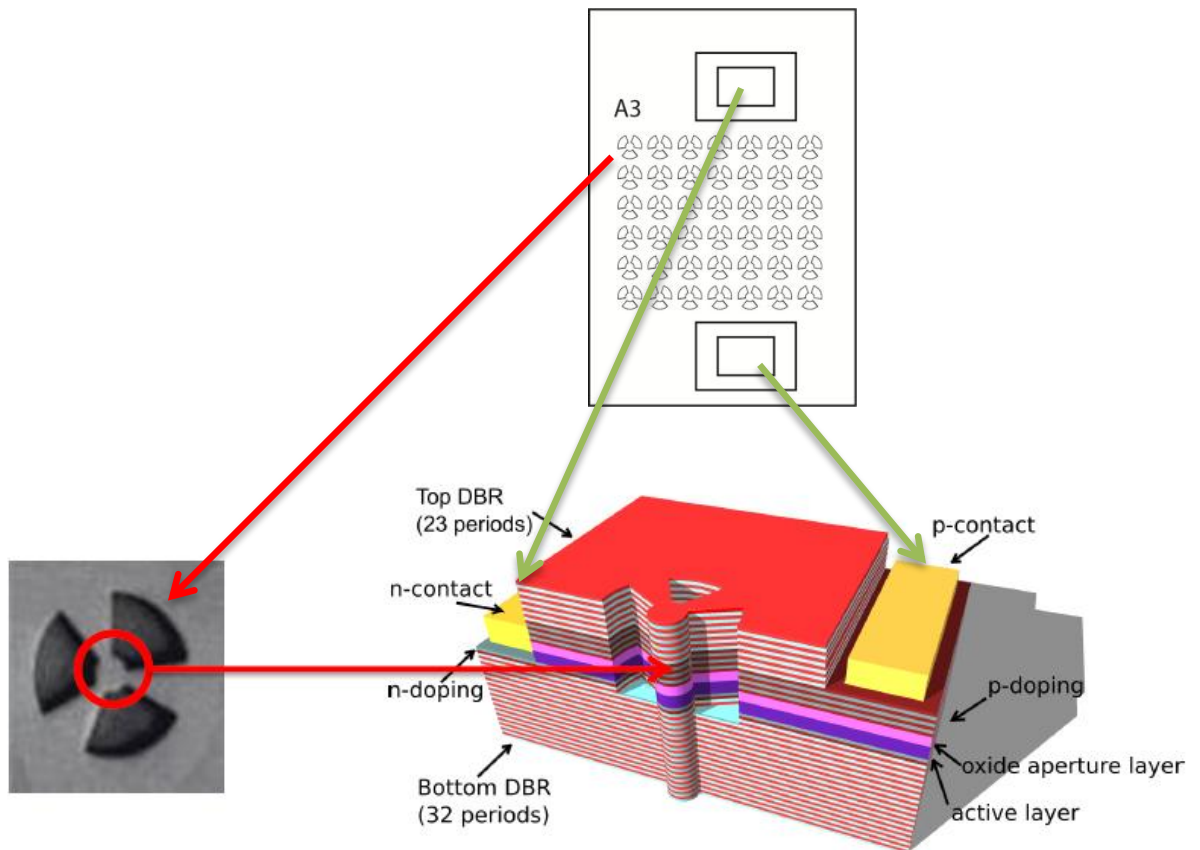
Figure 2.5: *Micropillar sample. There are contacts placed on the sample to create a PN-junctie. This allows to tune the quantum dot in resonance with the cavity. The indicated cavity is R1C1*

The samples are grown by Molecular Beam Epitaxy(MBE) and the QDs are grown following the Stranski-Krastanow method[12]. On a layer of GaAs there are In and As atoms dropped at very high temperatures. These atoms form atomic layers if the lattice mismatch between substrate and lattice is small enough. At a certain point, due to strain and surface energy, it becomes energetically favorable for the structure to form islands. These islands are the actual QDs. This is shown in Fig. 2.6 below. These QDs are often called InAs/GaAs QDs because

some of the Ga diffuses into the InAs. The density of the QDs can be varied on the same wafer using MBE. This allows for the creation of an array of samples with each a different QD density. Finally a layer of GaAs is grown over the InAs islands, Thus embedding the InAs/GaAs QDs inside the GaAs. This layer is called the active region.
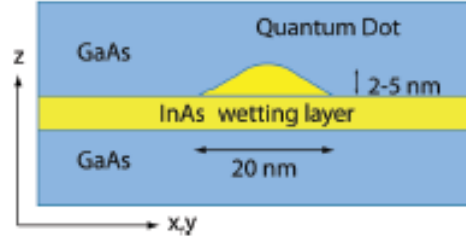

Figure 2.6: *Schematic picture of QD island. They are grown following the Stranski-Krastanow method.*

A micropillar cavity is formed around our quantum dot to enhance the optical interaction between a single quantum dot and an external optical mode. The complete structure of the micropillar is sketched in Fig. 2.7. The cavity consist of an active layer between two DBR-mirrors. A distributed Bragg reflector (DBR) is in our case a periodic structure formed in alternating layers of GaAs and $Al_{0.9}G_{0.1}As$. This gives a periodic variation in the refractive index in the sample. The lower DBR consists of 32 Bragg pairs and the upper DBR of 23 pairs. On top of the active layer there is an oxide aperture placed to confine the light in the transverse plane of the cavity. The position of the oxide aperture is place close to a node in the intracavity field, so that the absorption losses and scattering due to the aperture are minimal. To ensure optimal coupling of the QD excitons and the optical field, the electromagnetic wave has a maximum at the center of the active region where the QDs are placed.
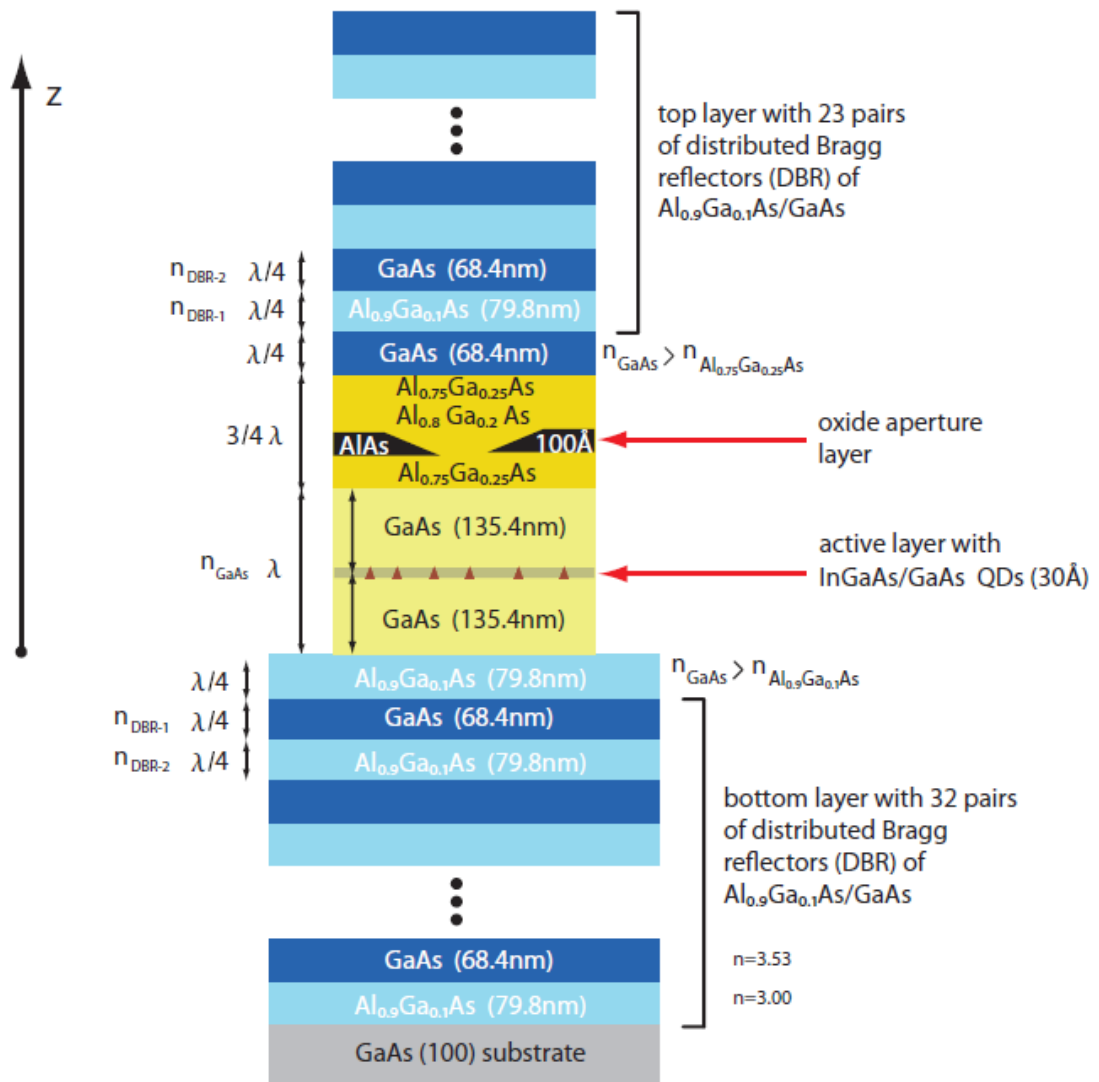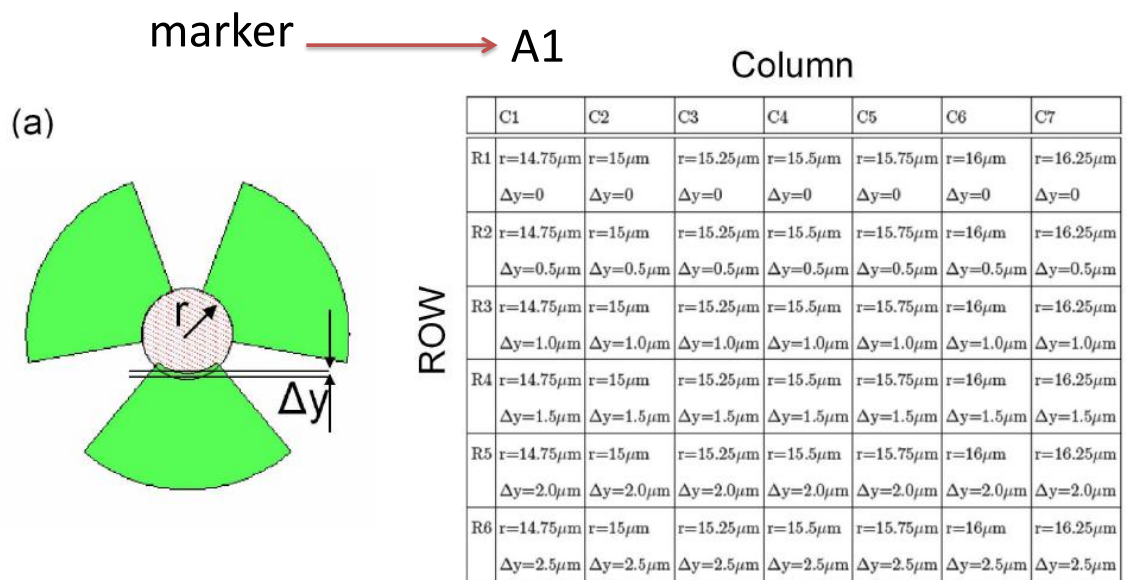
Figure 2.7: *The layer structure of the micropillar sample, Note the location of the oxide aperture layer and the quantum dots.*

In the sample there are three trenches etched from the top DBR down into the bottom DBR, making it possible to oxidize the AlAs layer. Here a wet lateral oxidation converts the $AlAs$ into Al_xO_x and thereby creates an oxidation front, leaving a small unoxidized area at the center. The difference in refractive index between the Al_2O_3 with $n = 1.77$ and the unoxidized AlAs $n = 2.93$ is approximately $\Delta n \approx 1.2$. In Fig.2.8 you see a schematic figure of the effective refractive index and a SEM picture of the oxidation front. The difference between the effective refractive index between the oxidized and unoxidized region is designed to be $\Delta n_{eff} = 0.08$ (see page 54 of [12]).
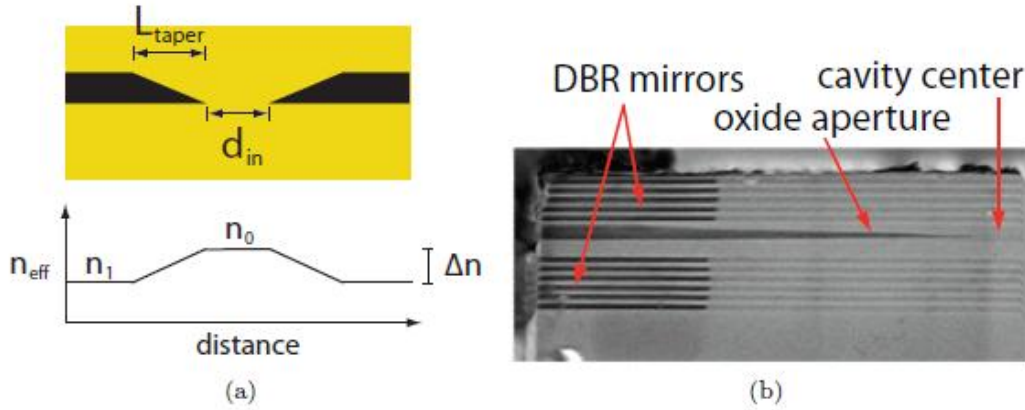
Figure 2.8: *a) Effective refractive index profile of the oxidation layer. b) SEM picture of the oxidation front. At the center of the cavity the oxidation front forms a sharp edge.*

The 42 cavities on the sample each have a different design see table in Fig.2.9, apart from the fact that they have small unintentional deviations due to the etching of the trenches. The cavities from the first column are designed to be round and have a radius ranging from 14.75 μm to 16.25 μm in steps of 0.25 μm. For the rows the middle trench is moved outward in steps of $\Delta y = 0.5$ μm. This is illustrated in Fig.2.9. We number the cavities as seen from the marker. So the cavity right under the marker in Fig.2.5 is R1C1. According to this the biggest cavity is R6C7. The reason for moving one trench outward is to compensate for the asymmetric oxidation rate of the aperture due to the crystal lattice structure of AlAs.

marker ——————→ A1

Column

(a)

ROW

	C1	C2	C3	C4	C5	C6	C7
R1	r=14.75μm Δy=0	r=15μm Δy=0	r=15.25μm Δy=0	r=15.5μm Δy=0	r=15.75μm Δy=0	r=16μm Δy=0	r=16.25μm Δy=0
R2	r=14.75μm Δy=0.5μm	r=15μm Δy=0.5μm	r=15.25μm Δy=0.5μm	r=15.5μm Δy=0.5μm	r=15.75μm Δy=0.5μm	r=16μm Δy=0.5μm	r=16.25μm Δy=0.5μm
R3	r=14.75μm Δy=1.0μm	r=15μm Δy=1.0μm	r=15.25μm Δy=1.0μm	r=15.5μm Δy=1.0μm	r=15.75μm Δy=1.0μm	r=16μm Δy=1.0μm	r=16.25μm Δy=1.0μm
R4	r=14.75μm Δy=1.5μm	r=15μm Δy=1.5μm	r=15.25μm Δy=1.5μm	r=15.5μm Δy=1.5μm	r=15.75μm Δy=1.5μm	r=16μm Δy=1.5μm	r=16.25μm Δy=1.5μm
R5	r=14.75μm Δy=2.0μm	r=15μm Δy=2.0μm	r=15.25μm Δy=2.0μm	r=15.5μm Δy=2.0μm	r=15.75μm Δy=2.0μm	r=16μm Δy=2.0μm	r=16.25μm Δy=2.0μm
R6	r=14.75μm Δy=2.5μm	r=15μm Δy=2.5μm	r=15.25μm Δy=2.5μm	r=15.5μm Δy=2.5μm	r=15.75μm Δy=2.5μm	r=16μm Δy=2.5μm	r=16.25μm Δy=2.5μm

Figure 2.9: *Sizes of each cavity. Each column increases the radius of the cavity by 0.25 micron and each row shifts one of the trenches each time 0.5 micron to the outside.[13]*

Chapter 3

Theory

3.1 Fabry-Perot cavity with absorber

Our samples can be modeled by a Fabry-Perot cavity with an absorber, where the DBR mirrors with the spacing layers form a cavity and the material absorbs. Suppose there are two plates a distance d from each other. The reflectivity of each plate is respectively $R1$ and $R2$. Plate 1 has a intensity transmission of $T_1 = 1 - R_1$. The absorption losses are included by R_{round}; this means that after one cycle in the cavity the intensity of the light is decreased by R_{round} due to absorbtion in the cavity. $R_{round} = 1$ means that the cavity has no losses due to absorption. The Fabry-Perot cavity is sketched in Fig.3.1.

Since the intensity $I = E^2$, this gives for the reflection of electric field $\sqrt{R} = r$ and $\sqrt{T} = t$. Finally this results in the following formula for the electric field in the cavity

$$E_{cav} = E_{in}t_1(1 + r_1r_2r_{round}e^{i\vartheta} + r_1^2r_2^2r_{round}^2e^{i2\vartheta} + ...) = E_{in}\frac{t_1}{1 - r_1r_2r_{round}e^{i\vartheta}}. \tag{3.1}$$

Here $\vartheta = 2k_0l_{cav}n_0$, where n is the refractive index between the mirrors. This represents the phase difference between each successive reflection.

This result can be rewritten in a much nicer way by rewriting $r_1r_2r_{round}$ as r and doing a Taylor expansion in the resonance region. So basically we assume $\vartheta \ll 1$, which gives
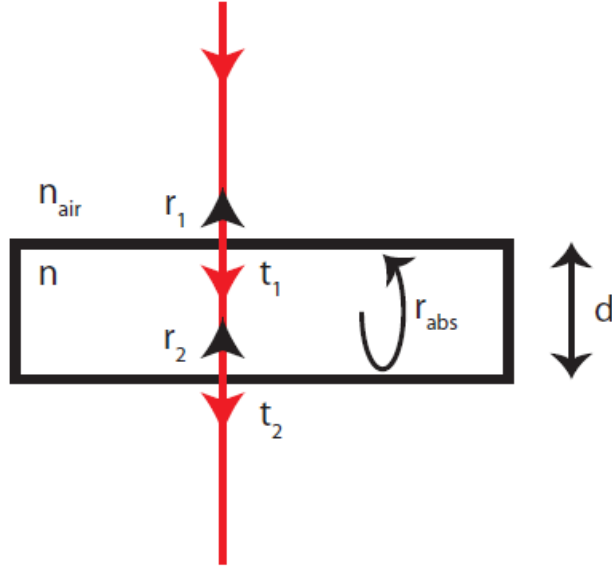
$$E_{cav} \approx E_{in}t_1\frac{1}{1 - r - ir\vartheta + r\frac{\vartheta^2}{2}}. \tag{3.2}$$

Now assume that the reflectivity of the mirrors is almost 1. So we set $r \approx 1$ to get

$$E_{cav} \approx E_{in}t_1\Big(\frac{\frac{1}{(1-r)}}{1 - \frac{r}{1-r}i\vartheta}\Big) \approx E_{in}t_1\Big(\frac{\frac{1}{(1-r)}}{1 - \frac{1}{1-r}i\vartheta}\Big). \tag{3.3}$$

Finally we fill in r to get formula 3.4 for the ratio between the incoupled light and the light that is in the cavity given by

$$\frac{E_{cav}}{E_{in}} \approx \frac{t_1}{(1 - r_1r_2r_{rond})}\frac{1}{1 - \frac{i\vartheta}{\Delta\vartheta}}, \tag{3.4}$$

Figure 3.1: *Fabry-Perot cavity. Here d is the distance between the two mirrors and n is the refractive index of the medium. r and t are respectively reflection and transmission coefficient respectively.*

with $\Delta\vartheta = (1 - r_1 r_2 r_{rond})$. This is the width of the resonance and is related to the full width half maximum as $FWHM = 2\Delta\vartheta$. Likewise the intracavity intensity at fixed input powers scales with

$$I_{cav}(\theta) \sim \frac{1}{1 + \frac{\vartheta^2}{(\Delta\vartheta)^2}} \tag{3.5}$$

So if the absorption increases then the width of the resonance will increase, which is equivalent to a decrease of the Q-factor. We measure the reflected light from the cavity so we are interested in

$$\frac{E_{reflected}}{E_{in}} = -r_1 + (t_1)(\frac{E_{cav}}{E_{in}}) = -r_1 + \frac{t_1^2}{(1 - r_1 r_2 r_{round})} \frac{1}{1 - \frac{i\vartheta}{\Delta\vartheta}}. \tag{3.6}$$

Using $r_1 = \sqrt{R_1} = \sqrt{1 - T_1} \approx 1 - \frac{(t_1)^2}{2} \approx 1$, and $r_1 r_2 r_{round} = 1 - \frac{1}{2}(t_1^2 + t_2^2 + t_r^2)$, we get

$$\frac{E_{reflected}}{E_{in}} = -1 + \frac{2t_1^2}{(t_1^2 + t_2^2 + t_{round}^2)} \frac{1}{1 - \frac{i\vartheta}{\Delta\vartheta}}. \tag{3.7}$$

The term $\frac{2t_1^2}{(t_1^2 t_2^2 t_{round}^2)}$ describes the ratio of intensity losses. So to increase the contrast observed in the reflection we should have $t_{round} << t_1, t_2$ and $t_1 \simeq t_2$. This is not the case in the cavities,

because our top layer has 23 pairs of DBR layers and the bottom layer has 32 pairs of DBR-layers. So we would not get a maximum contrast. The maximum resonant reflectivity of our bottom DBR is given by

$$r_{dbr} = \frac{1 - (n_{GaAs}/n_{AlGaAs})^{2p}}{1 + (n_{GaAs}/n_{AlGaAs})^{2p}}. \tag{3.8}$$

For the top DBR the formula is different, because begin and end medium are then different. There two extra constants added, one constant before each $(n_{GaAs}/n_{AlGaAs})^{2p}$) term. In our case the reflectivity of the mirrors is greater than 99%. Each layer has a optical thickness of one-quarter wavelength, because then due to constructive interference the layers act as high-quality reflectors. The range of wavelengths that is reflected is called the photonic stop band. A simulation of the reflection spectrum is shown in Fig.3.2
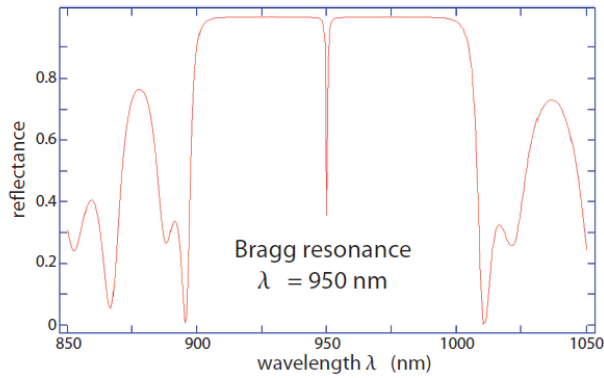
Figure 3.2: *reflection spectrum of the design of a cavity with Bragg resonance at 950 nm.*

To visualize the oxidation taper we can look at the change of the side lobes as shown in Fig.3.2. Due to the oxidation there the refractive index of the material will change. As a result the reflectivity of the side lobes is different for certain wavelengths between an oxidized and unoxidized region. This difference in contrast is shown in Fig.3.3.

Not only will the taper oxidize, but also the layer of AlGaAs will oxidize a bit. In Fig.3.3c and Fig.3.3d you see that oxidation of the mirrors has an enormous effect on the reflectivity of the side lobes. In Fig.3.3d all the mirror layers are oxidized. In reality this never happens because GaAs does not oxidize very quickly. In Fig.3.3c and d we did not account for the fact that the trench did not go through all the mirrors. So the last few DBR layers cannot be oxidized. The effect of this is not very big and will not give a big change in contrast. A side lobe at a large wavelength was chosen, because the side lobes at a smaller wavelength will disappear at higher temperatures. This disappearance at high temperatures happens due to absorption of the bandgap that red shifts. That is why there is then almost no change in side lobes contrast. The effect of doping and absorption, mostly due to the bandgap, was not accounted for in Fig.3.3.
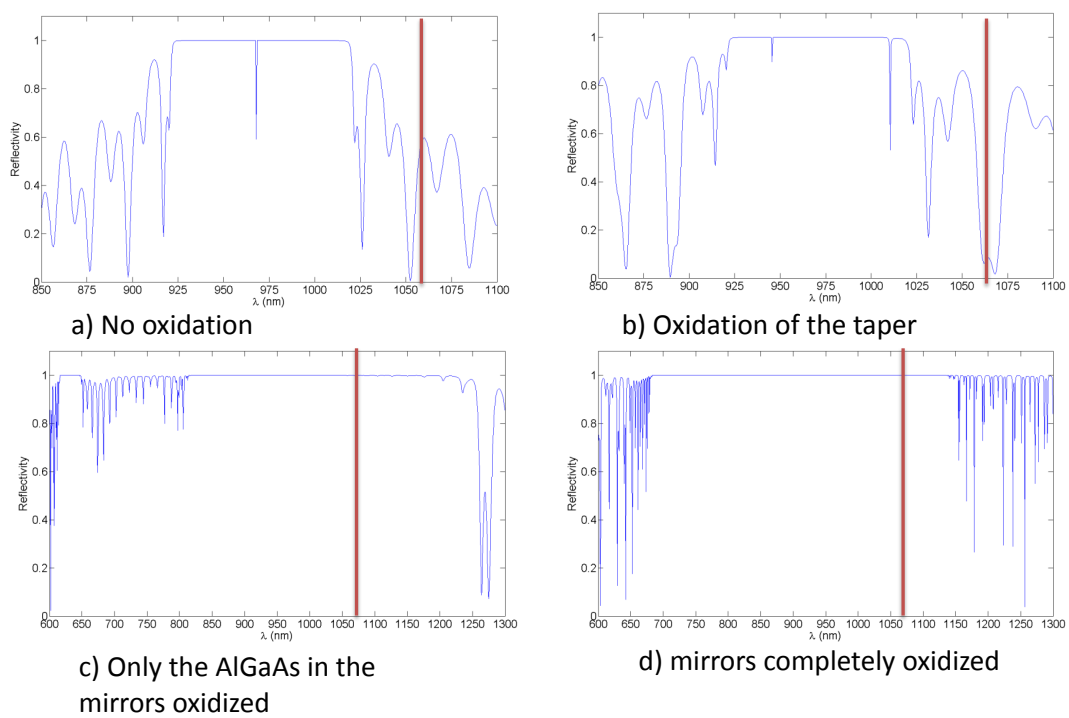
Figure 3.3: *Calculated spectra of the expected reflection spectrum at 20°C. Not accounted for are absorption and doping of some layers. a)Reflectivity of the mirrors with nothing oxidized. b)Only the taper(AlAs)is oxidized. c)The AlGaAs layers in the mirrors and the taper is oxidized. d)The mirrors and tapers are all oxidized*

Summarizing the result from Fig.3.3, we can predict of how the reflection of the cavity looks like at a wavelength 1064 nm at room temperature. There should be an average reflective circle at the center, then a very low reflective donut. Around the donut is an almost 100% reflective red layer, which represents the oxidized mirrors. The unoxidized trenches are also blue due to a side lobe in the reflection spectrum of the mirror that is left. This is shown in Fig.3.4.
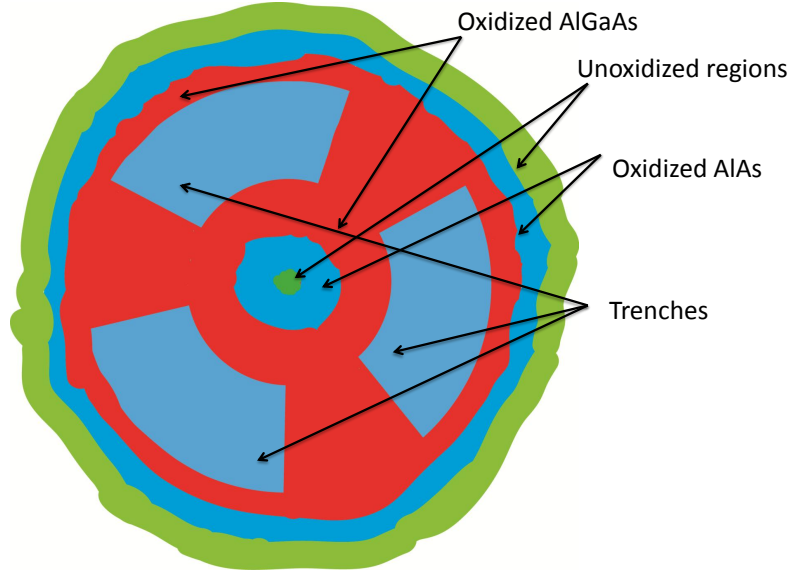
Figure 3.4: *Expected ideal intensity profile from reflection at 1064 nm from a cavity. Red corresponds to a high reflectivity, blue a low reflectivity and green an average reflectivity.*

3.2   Coupling of light into a cavity mode

If the light is confined in the cavity due to the aperture we measure the transverse mode of a beam. So the electrical field pattern of the beam is measured in the plane perpendicular to the direction of the beam. In order to describe the optical modes we assume an isotropic material with a quadratic refractive index profile. With an isotropic material this would give the wave equation shown as equation 3.9. Finding the solution of the wave equation gives the optical modes in the cavities.

$$\nabla^2 \mathbf{E}(\mathbf{r}) + k_0^2 n^2(\mathbf{r})\mathbf{E}(\mathbf{r}) = 0 \tag{3.9}$$

Here $\mathbf{E}$ is the electric field, k_0 wavenumber in vacuum, and $n(\mathbf{r})$ is the refractive index distribution. In addition the index is given by

$$n(\mathbf{r}) = n^2(x,y) = n_0^2(1 - \frac{x^2}{r_x^2} - \frac{y^2}{r_y^2}) \tag{3.10}$$

where $r_{x,y}$ accounts for the rotational asymmetry of the aperture.

Detailed analysis of the solution of equation (3.9) is given in the bachelor thesis of Keesjan de Vries[14]. The solution of the wave equation (3.9) are Hermite Gaussian modes of the form

$$\psi_{[nm]}(x,y) = H_n(\frac{\sqrt{2}x}{w_x})H_m(\frac{\sqrt{2}y}{w_y})e^{-(\frac{x^2}{w_x^2}+\frac{y^2}{w_y^2})}, \tag{3.11}$$

where $w_x = w_y = \sqrt{\frac{2r_{x,y}}{k}}$. Knowing this and assuming that the light from our single mode fiber is a gaussian beam the coupling efficiency η_{nm} can be calculated using formula

$$\eta_{nm} = \frac{\mid \int dA\psi_{nm}\psi_{in}^* \mid}{\int dA\psi_{nm}\psi_{nm}^* \int dA\psi_{in}\psi_{in}^*}, \tag{3.12}$$

where ψ_{in} is the incoming Gaussian beam and where the (two-fold) integration runs over the transverse area dA = dxdy. The first few Hermite Gaussian modes are shown in Fig.3.5. We took here a spot size of 0.3 μm and predefined a small cavity of $w_x = w_y = 1$ μm. The $\psi_{[20]}$ mode has three blobs of high intensity. If we take a spot size larger than the cavity fundamental waist the central blob of $\psi_{[20]}$ will almost completely disappear.
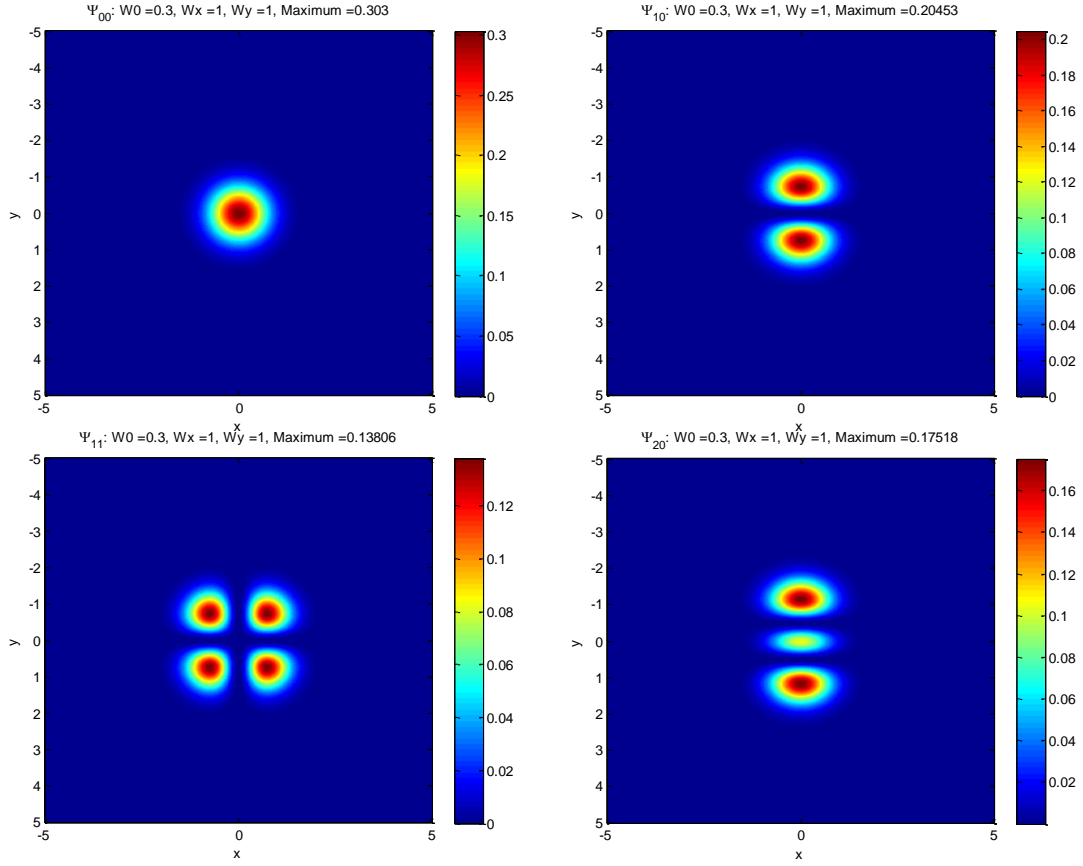
Figure 3.5: *Assuming an aperture of $w_x = w_y = 1\mu m$ and a spot size radius of 0.3μm. The red areas correspond to the highest coupling efficiency.*

The optimal coupling spot size for a given cavity with a fundamental waist of $1\mu m$ is different for each mode as shown in Fig.3.6. For the fundamental mode the maximal coupling for a cavity with a radius of 1 μm is obviously 1 (modematched). To excite and observe the higher order modes you may want to make your spot smaller. The main goal of this figure was to find the optimal spot size to get a good contrast for the fundamental and first-order mode. So that the splitting between these two could give a measure of how big the region is which is not oxidized. In this case the optimal spot size would be 0.9 μm. In reality the size of the aperture is not known so a telescope is used to vary the size of the spot.
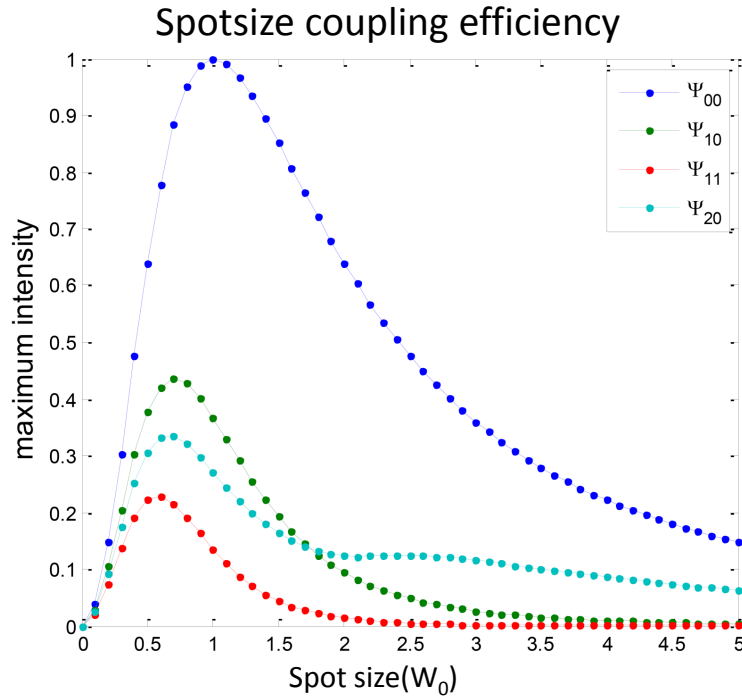
Figure 3.6: *Coupling efficiency for the first few modes as function of the gaussian incoupling spot. The cavity has a fundamental mode width of $w_x = w_y = 1\mu m$.*

3.3 Influence of high temperatures on cavities

The main changes in the cavity due to the increase in temperature will be (i) the thermal expansion, (ii) an increase in the refractive index of the materials, (iii) and a decrease of the bandgap energy of GaAs at higher temperatures. These changes of the cavity have three effects:

1. red shift of the cavity resonance,

2. increased absorption (due to the bandgap),

3. as a result, reduced Purcell factor.

**Red shift of cavity resonance**

(i) and (ii) will result in a red shift of the cavity modes. (i) Will red shift the cavity modes due to an increase in the length of the cavity. (ii) red shifts the cavity modes, because the resonant wavelength changes with the refractive index of the material. The refractive index is the factor by which the wavelength and the velocity of the radiation are reduced with respect to their vacuum values.

Increased absorption

(iii) results in more absorption and other non-radiative processes becoming more dominant. The bandgap is an energy range in a solid where no electron states exist. The bandgap refers to the energy difference between the top of the valence band and the bottom of the conduction band. When the temperature increases the amplitude of atomic vibrations increases, which leads to a large interatomic spacing. An increased interatomic spacing decreases the potential seen by the electrons in the material, which in turn reduces the size of the energy bandgap[15]. The relationship between the bandgap and temperature is described by Varshni's empirical expression[16].

$$E_g(T) = E_g(0) - \frac{\alpha T^2}{T + \beta} \tag{3.13}$$

Where α, β and $E_g(0)$ are material constants. The Varshni expression shows a decrease of the bandgap energy. Filling in the constants [17] for GaAs gives Fig.3.7. Which shows that at higher temperatures the absorption of the bandgap increases and non-radiative processes become more dominant.
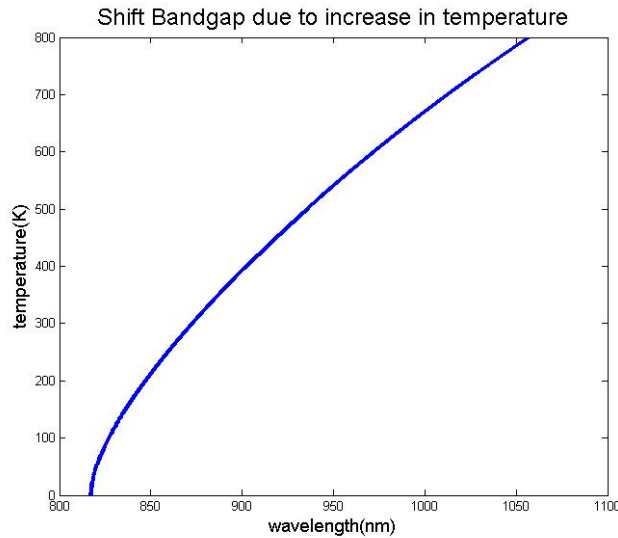
Figure 3.7: *Shift of the bandgap due to increase in the temperature. Up to 700k there is no absorption of the bandgap at 1064nm.*

Reduced Purcell factor

At high temperatures the Purcell factor will decrease a bit through the increase in effective volume. Although it is mostly the Q-factor that will decrease as a result of increased absorption of the bandgap. The Purcell factor F_P is the ratio between the cavity transition rate and the free-space transition rate for spontaneous emission. With the quantum dot in resonance with the cavity the Purcell factor becomes

$$F_P = \frac{\omega_{cav}}{\omega_{free}} = \frac{3Q}{4\pi^2 V_0}(\frac{\lambda}{n})^3. \tag{3.14}$$

Here Q is the quality factor of the cavity and V_0 is the cavities effective mode volume. A derivation of equation (3.14) can be found on page 40 of Jan Gudats Thesis [12]. As a result of this lower Purcell factor, the coupling of the external mode to the cavity becomes worse.
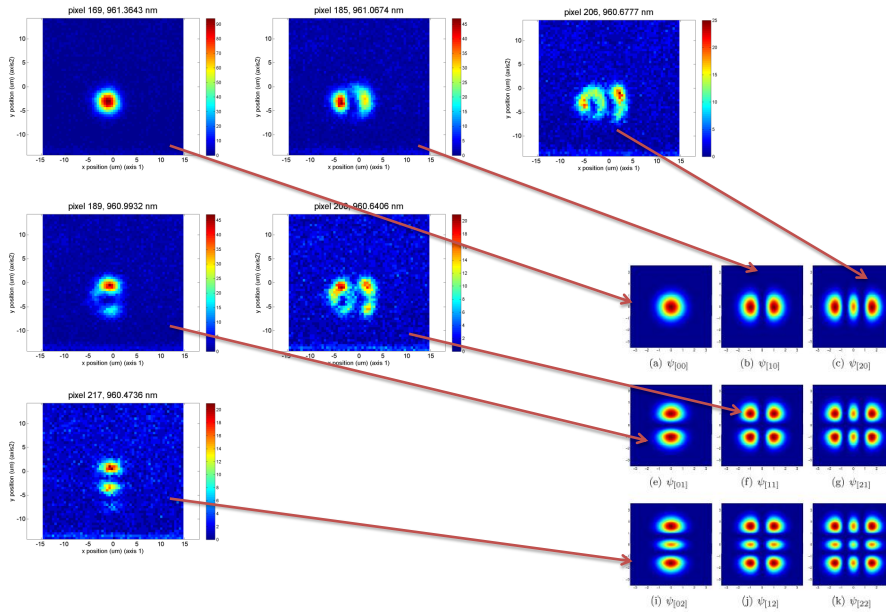
Chapter 4

Photoluminescence

4.1 Characterization of the cavity modes

The photoluminescence (PL) measurement results on an oxidized sample at room temperature are presented in Fig.4.1.


Figure 4.1: *The modes measured in a cavity at room temperature. Red corresponds to a high intensity and blue a low intensity. In the bottom right corner the examples of the theoretical Hermite Gaussians with $w_x = w_y = 1/\sqrt{2}$ in equation 3.11 are shown. These pictures are taken while coupling in with single-mode and the light is collected using a multi-mode fiber (core 62.5 µm).*

During PL measurements the sample is illuminated by light of a pump (780 nm) that has an higher energy than the energy of the bandgap of (860 nm). This way electrons can be excited

across the bandgap. When an electron recombines with a hole a photon will be emitted. The electrons and holes relax into the QDs due to diffusion and energy loss. Over the entire sample are QDs at different wavelengths, but the QD emission is collected more efficiently if it couples to a cavity mode, making the cavity modes visible. The first 6 Hermite Gaussian where visible as shown in Fig.4.1. In the pictures from Fig.4.1 we measure as function of the position at a fixed wavelength. We have corrected for the number of darkcounts. These arise due to the electronics in the CCD-camera. The integration time for the spectrometer for these measurements was 1 second with a (x,y) position scan of 60 by 60 steps and with a step size of $0.5\mu m$.

In Fig.4.2 you see the spectrum of the DBR-resonance. For a position next to the cavity you still have two mirrors which form a Fabry-Perot interferometer. Only there is no oxidized aperture present as in the cavities. There are of course still quantum dots who emit light and it is this light which is measured with the spectrometer. The integration time for the spectrometer for these measurements was 1 second. The same combination of fibers is used here as in Fig.4.1.
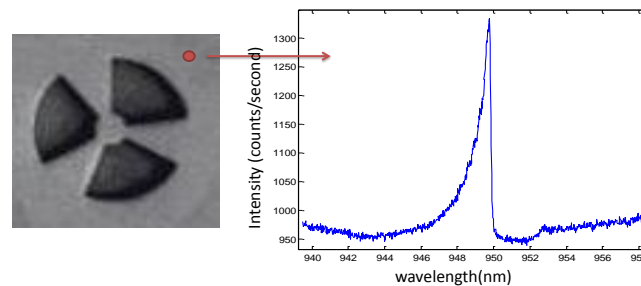

Figure 4.2: *The spectrum of the DBR-cavity observed at room temperature for a position next to the cavities on the sample, there is no correction for the number of darkcounts.*

4.2   Temperature dependence

To check if the DBR-resonance and cavity modes are indeed no longer visible at higher temperatures using PL, we measured the wavelength shift and change in intensity as function of the temperature of the DBR-resonance. The DBR-resonance was measured because it had a better visibility than the fundamental cavity mode. The result is shown in Fig.4.3. In the left figure of Fig.4.3 the shift of the wavelength as function of temperature is visible and in the right figure you see how the intensity of the DBR-resonance decreases as function of the temperature. At $20\,^{\circ}\mathrm{C}$ we measured an intensity of 100 counts/second but at $250\,^{\circ}\mathrm{C}$ only 10 counts were left. This makes measurements at higher temperatures impossible. The decrease in intensity can be explained by the increased absorption originated from the shift of the bandgap at higher temperatures see Fig.3.7. From Fig.4.3 we estimate that from $30\,^{\circ}\mathrm{C}$ tot $230\,^{\circ}\mathrm{C}$ the wavelength red shifts about 20 nm ± 2 nm, which corresponds to a relative increase

in wavelength of $2.1\% \pm 0.2\%$. Below we will explain that this shift agrees with theoretical expectations.
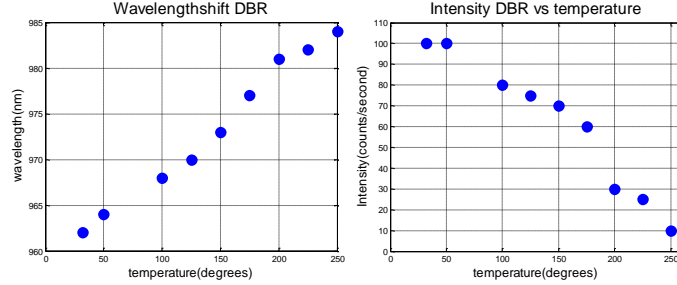
Figure 4.3: *The wavelength shift(left) and the decrease of intensity of the DBR-resonance as function of temperature(right).*

As a first-order approximation we can explain this shift by an increase in the refractive index. A change due to thermal expansion is not taken into account, because it is very small according to [17]. The thermal coëfficient for linear expansion is $5.73 * 10^{-6 \circ} C^{-1}$ this would increase the length of a layer of GaAs by only 0.2% for a temperature increase of 400 °C. The values for the refractive index are taken from [18]. In Fig.4.4 the normalized increase in refractive index is shown for GaAs and AlGaAs. Both are normalized to 1 for 300K.
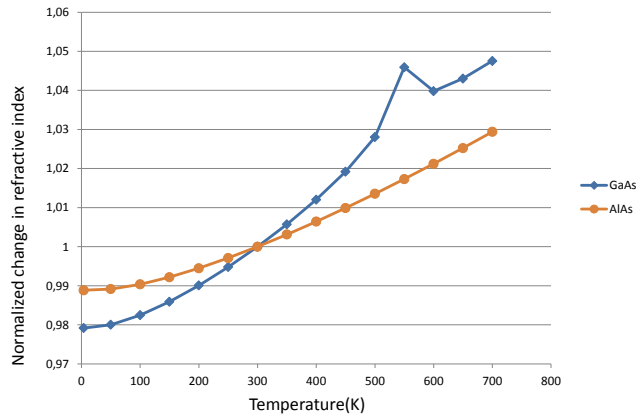
Figure 4.4: *Increase in refractive index for GaAs and AlAs. Both graphs are normalized with respect to 1 for 300K.*

Changing the refractive index by varying the temperature from 30 °C tot 230 °C, which is from 300K tot 500K in Fig.4.4, will result in an increase of the refractive index. For GaAs there is an increase of the refractive index of 2.8% and for AlAs there is an increase of 1.4%. The actual red shift will be somewhere in between these values. To first order this agrees with the measured red shift of 2.1%. Fig.4.3 shows that at 250 °C the DBR has a wavelength of

985 nm. If we extrapolate this, by assuming a linear behavior, then resonance wavelength will be 1005 nm at an oxidation temperature of 400 °C. At 400 °C the bandgap has red shifted to 1000 nm making measurements at high temperatures impossible. The reason that the cavity modes disappear already at lower temperatures happens, because a little bit absorption from the tails could let the signal disappear. Additionally there could be absorption by acceptor or donor states inside the bandgap. Also in PL is an extra spectral feature visible outside the bandgap of GaAs. If this spectral feature shifts with the same speed as the bandgap, then the cavity modes can indeed already disappear at 250 °C.

Chapter 5

Resonant broadband reflection

5.1 Characterization of the cavity modes

With a reflection measurement we measure the light which is reflected from the sample. The light on the sample is injected through a single mode fiber and also detected with one. We then scan the sample in the x and y direction. The wavelength range is 19 nm with a spectral range of 0.019 nm per pixel.

A3R1C6 (oxidized,4x telescope)
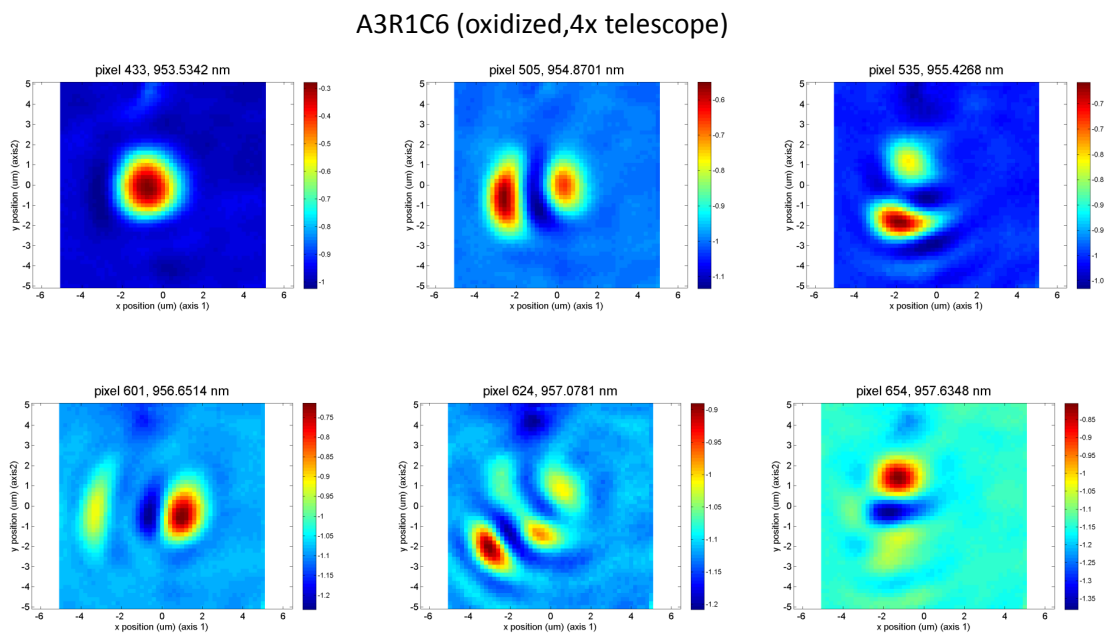
Figure 5.1: *False-color pictures of reflection measurements taken at different wavelengths versus (x,y) position on the sample. Red corresponds to a low reflectivity and blue to a high reflectivity*

If the light couples resonantly into the cavity, then the reflection is a lot less. As a result we

see dips in the reflectivity at specific wavelengths which represent the cavity modes. For all the reflection measurements we used an integration time of 0.01 second. The fundamental and first-order modes are visible in Fig.5.1. The two first-order modes (top row middle and right) are not symmetric, probably because the incoupling is not ideally perpendicular to the sample surface and the cavity is not perfectly symmetric. The second-order mode (3 pictures in bottom row) misses some contrast dips, this is not very strange because the coupling prediction in section 3.2 showed a very low intensity for the center blob. If light was coupled in with a spot size bigger than the aperture of the cavity, then the central blob will not be visible anymore.

Reflection dips are also observed for DBR without lateral confinement. As shown in Fig.5.2 these dips are asymmetric and have a small reflection compared to the fundamental mode of a cavity. The reflection is asymmetric because the DBR-resonance consist of a lot of modes which are added together. The reflection is smaller compared to the fundamental mode because there is for the DBR no lateral confinement. A third behavior of the DBR
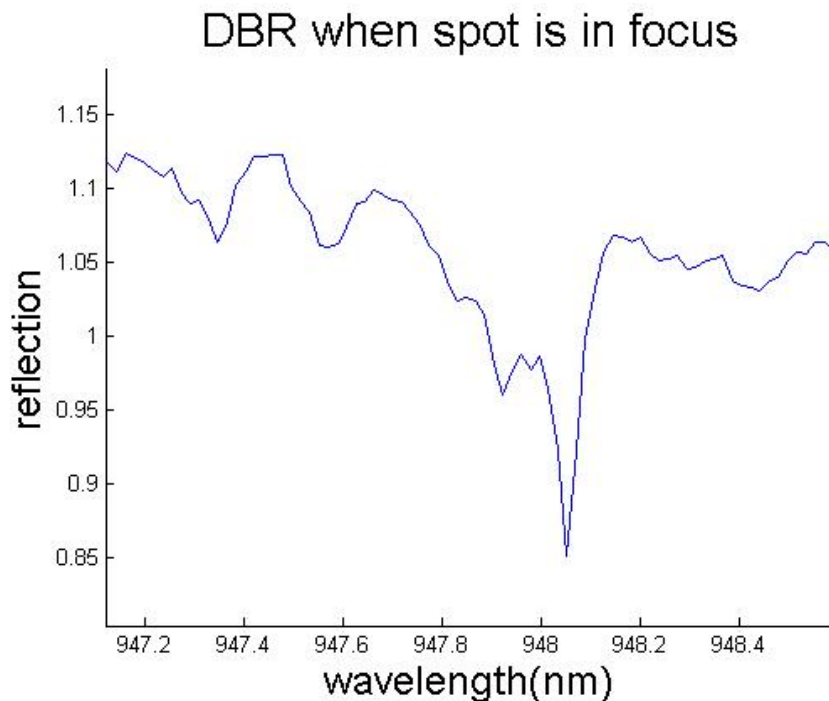
Figure 5.2: *Reflection of the DBR gives a reflection dip of about 15%, while reflection of the fundamental mode gives a reflection dip of 40% (see Fig.5.4).*

we found was that it showed oscillations as shown in Fig.5.3. These oscillations appeared only when we moved the sample towards the objective and as result the spot out of focus. Moving the sample away from the objective did not give any oscillations. These oscillation probably appear due to direction in which the light hits the objective and how the light fills the entrance of the objective.
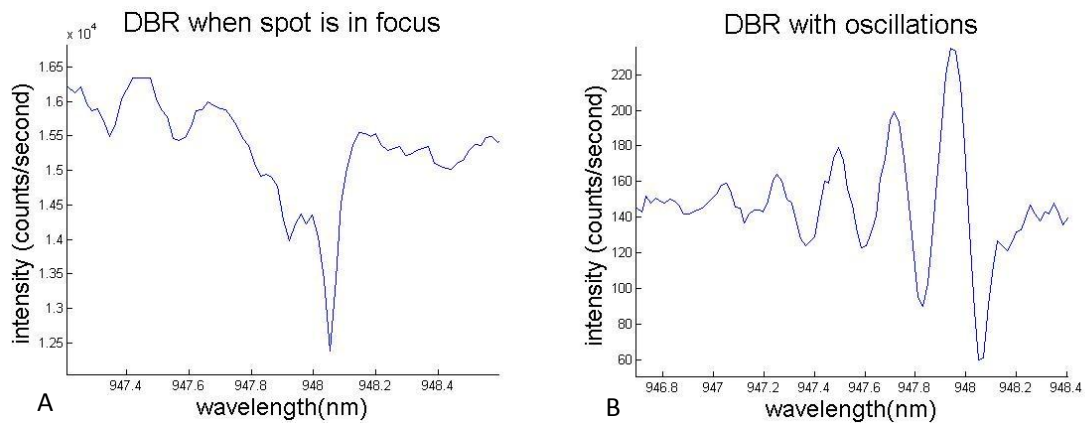
Figure 5.3: *Behavior of the DBR. a) Shows the DBR when spot is in focus, b) Shows the oscillations of the DBR. In b) is the number of counts per second very low compared to a.*

5.2   Temperature dependence

To get an optimum contrast it was useful to measure the fundamental mode as a function of temperature. This is shown in Fig.5.4. The Reflection dips of the fundamental mode are normalized with respect to the average reflection of the sides of the fundamental reflection dip. So a reference spectrum was not used. To make sure we had a reasonable horizontal and flat line at both sides of the fundamental mode we used a $\lambda/2$-waveplate to change the polarization dependent grating of the spectrometer.
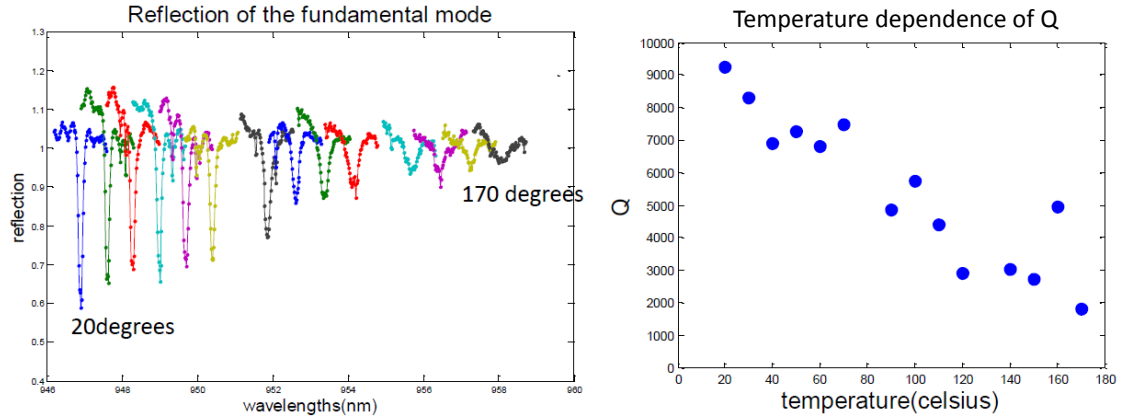
Figure 5.4: *Temperature dependence of the reflection dip associated with the fundamental mode. (left) Reflection spectrum and (right) quality factor Q deduced from that spectrum. In the left figure is the reflection of the fundamental mode vs temperature shown and in the right figure is the Q versus the temperature shown.*

With an increase in temperature we see a decrease of the contrast and the Q-factor. The Q-factor is estimated by doing a lorentzian fit on the fundamental modes. This measurement was done with a sample with cavity modes which were visible at room temperature. At $20\,^{\circ}\mathrm{C}$ we measured a Q $\approx$ 9000, but at $170\,^{\circ}\mathrm{C}$ we had only a Q $\approx$ 1000 left. The decrease of the Q indicates that there is absorption of the bandgap at the cavity wavelength. Although the cavity modes disappear already before $200\,^{\circ}\mathrm{C}$ might not be entirely due to the bandgap. At least we know for sure that at $420\,^{\circ}\mathrm{C}$ the bandgap will absorb all the signal because of the earlier calculated shift in section 4.2.

## 5.3   Background of the reflection

In the background of the reflection spectrum, there are some wavelength dips due to absorption. This is especially visible for wavelengths around 940 nm as shown in Fig.5.5. These lines probably appear due to the absorption of vibrational excitations in water[19],[20]. This is the water in the air around the optical part of the setup because at 400 degrees the absorption lines are still exactly on the same place as shown in Fig.5.5.
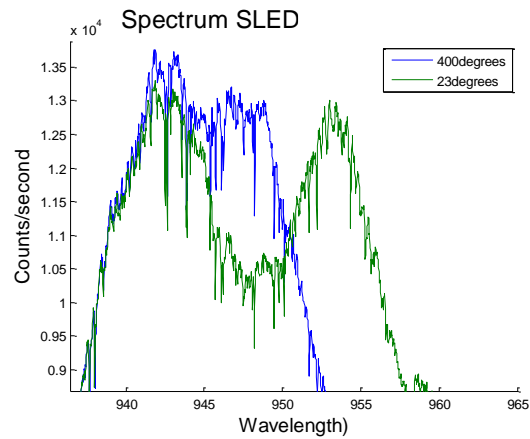
Figure 5.5: *Here is the spectrum of the SLED at 400°C and 23°C for the region where the cavity modes should appear on the photonic stop band. The absorption lines remain on exactly the same place. The difference in the contrast is probably due to a difference in the focussing of the SLED light.*

5.4   Agreement between photoluminescence and reflection

This short section shows the agreement between the PL and RF measurements, simply to prove that the cavity modes we measure using PL are the same as those when using reflection. This is done in Fig.5.6 by looking at the splitting between the modes. The splitting between the fundamental and first order mode was about 2 nm for the cavity used for Fig.5.6. The modes which are mainly visible here are the fundamental and a second order mode. The distance between the PL peaks and the RF dips agree very well to each other. These spectra were taken when the fundamental mode was optimally excited. This is why the odd higher order modes are not visible, but this allows us to stay approximately on the exact same place on the cavity. So that the incoupling in the case of reflection is optimal for the fundamental mode.
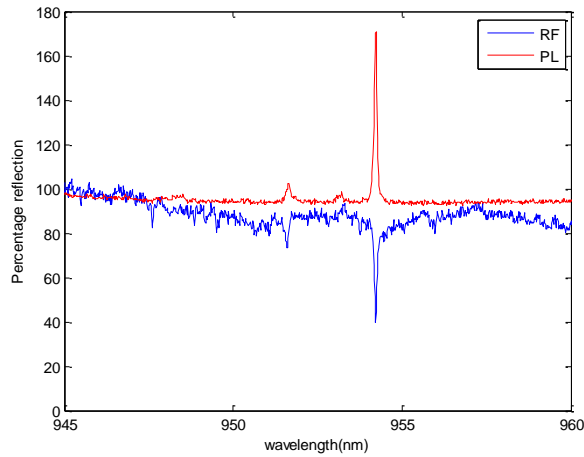

Figure 5.6: *This spectra shows that the modes we measure using PL and RF agree very good with each other. The reflection is shown in blue and the PL-result is shown in red. The cavity used here had a splitting between the fundamental and first mode of about 2 nm.*

Chapter 6

Side lobe reflection at 1064 nm

6.1 Oxide aperture probing

Another way of monitoring the oxidation was looking at the spectral side lobes beyond the stopband of the DBR mirrors. Specifically the side lobes at a long wavelength range, because these are not influenced by absorption of the bandgap. As shown in the theory section, at 1064 nm there was a good contrast between the side lobes of the oxidized and unoxidized layer. After oxidizing a sample called A1 at $420\,^{\circ}$C for 40 min. We had a splitting of 0.26 nm for the cavity modes at cavity R1C1. The reflection of the side lobe of cavity R6C1, which was oxidized simultaneously and probably had splitting a little bit smaller than R1C1, is shown at room temperature in Fig.6.1a.
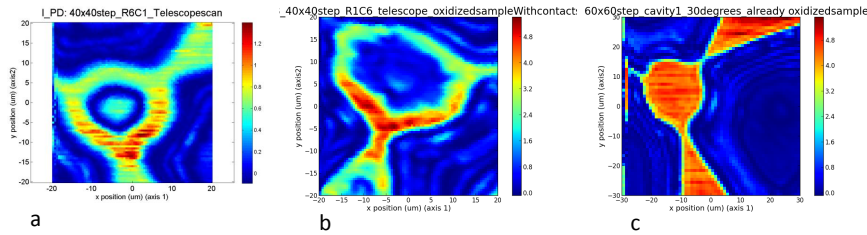

Figure 6.1: *False color plots of the position dependence of the reflectivity at λ=1064 nm. a) Underoxidized cavity with a splitting around 0.26 nm. b) Overoxidized cavity with splitting of splitting of 2 nm. c) Extremely overoxidized cavity with even the mirror layers are completely oxidized.*

The blue region of the oxidation taper is clearly visible, just as the unoxidized part in the center. Also the red part around the trenches, which represent the parts where the mirror is oxidized is visible. Fig.6.1a agrees well with Fig.3.4 from the theory. In Fig.6.1b you see an overoxidized cavity. The cavity modes are still visible for this device and the splitting between the fundamental and first order mode is around 2nm. In Fig.6.1c you see a extremely overoxidized cavity. The red area indicates that the mirrors are completely oxidized and no cavity modes could be observed.

6.2   Temperature dependence

**Temperature dependence from the reflection of the side lobes.**
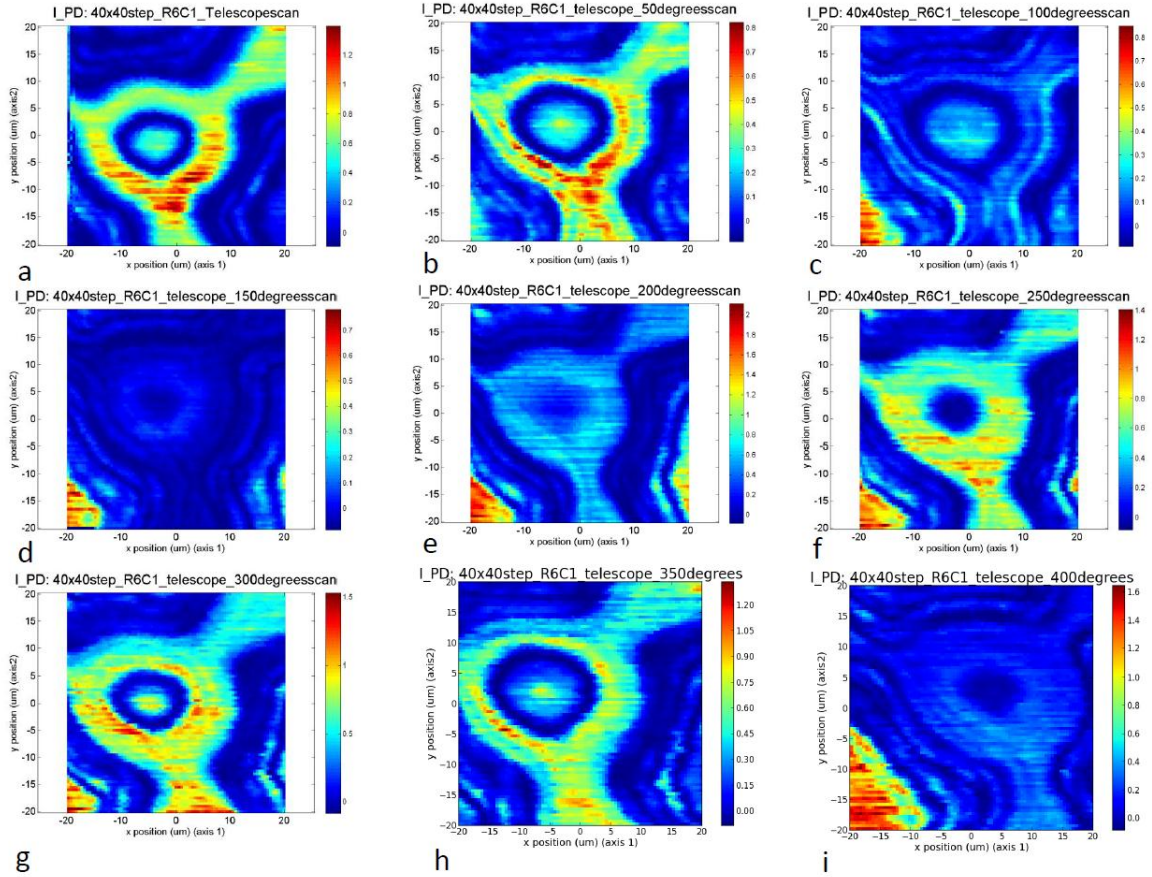
Figure 6.2: *shows for different temperatures the reflection of 1064 nm light on cavity R6C1. Red is very high reflection and blue is a very low reflection. a) is for a temperature of 20°C. For b to i the temperature increases from 50°C to 400°C in steps of 50°C (see figures).*

The side lobes in the reflection spectrum will change with wavelength if you increase the temperature. So the intensity of the reflected light at 1064 nm will change with temperature. This is shown in Figure 6.2a-i on an underoxidized cavity. We see a recurring pattern which you would expect because a low reflectivity can only become higher and and high reflectivity can only become lower. This can be seen in Fig.3.3. It is important to know what the temperature dependence of the side lobes is, because of the big influence on the contrast. So further research is needed to find a good compromise, between the oxidation temperature and the temperature where the reflection gives a well-defined contrast.

Chapter 7

Real-time monitoring

Fig.7.1 shows the result of oxidizing a sample at 420 °C. The blue region is the oxidation
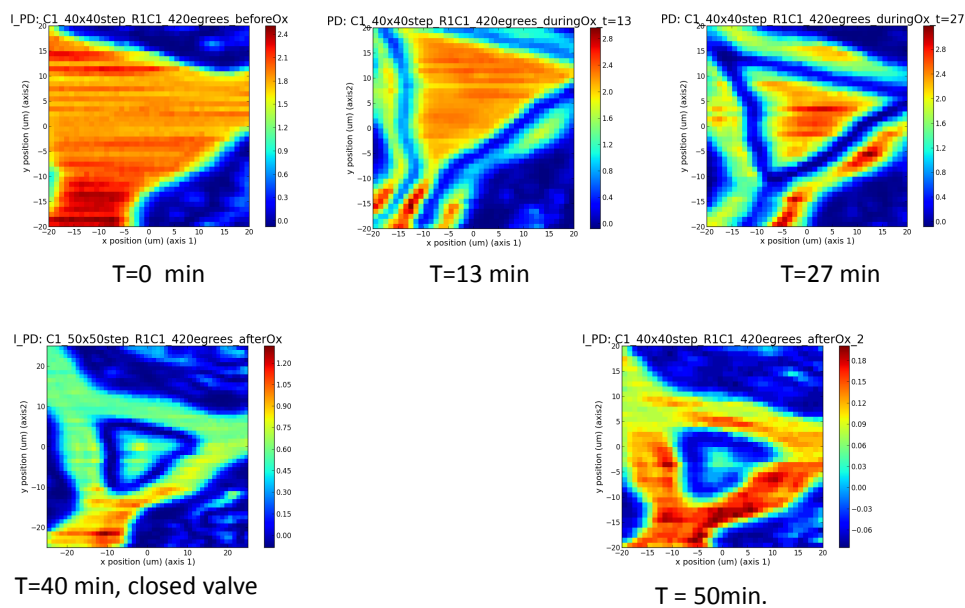
Figure 7.1: *Real-time monitoring of the oxidation of the cavity through reflection measurements. The shift of the oxidation taper (blue region) is clearly visible. After closing the valve at 40min the oxidation still continued for 10 minutes due to water in the material.*

taper which is moving towards the center. In the beginning the oxidation taper looks like a triangle, but at the end it becomes more circular with an unoxidized circular plane left in the

center. After 40 min we closed the valve so that the oxidation would stop, but due to water still in the sample the oxidation still continued, so the center region kept shrinking. We ended the oxidation by cooling down the sample completely. With the chosen settings it took about 6 minutes to take each picture.

After oxidizing and cooling down the sample we looked at the cavity modes. The splitting between the fundamental and first order mode was 1.3 nm. However, the modes visible in Fig.7.2a and b look ugly. The fundamental mode doesn't look circular at all. Fig.7.2c shows the fundamental mode as function of the wavelength. Fitting the fundamental mode with a Lorentzian gives a Q ≈ 7000 for this cavity.
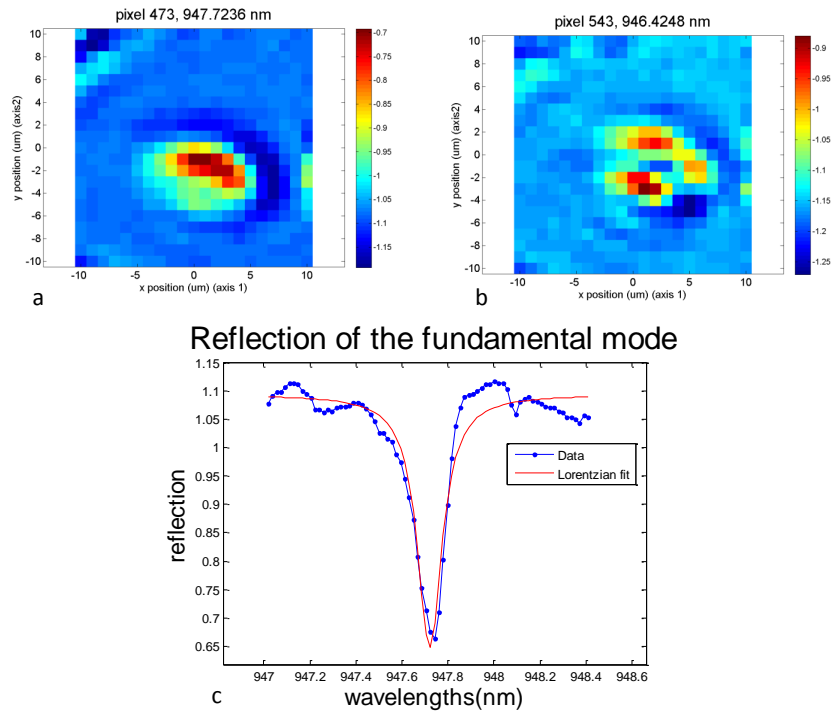
Figure 7.2: *Reflection pattern of an oxidized sample. In a) the fundamental mode is visible, where red is a low reflectivity and blue a high reflectivity. b) shows the first first-order mode. And c) shows the fundamental mode as function of wavelength. Fitting it with a lorentzian gives a Q ≈ 7000.*

A strange thing that happened after oxidizing the sample was that the cavity modes were extremely blue shifted with respect to the DBR. The DBR mode was found at 965nm while the fundamental cavity mode was found at 947 nm. This shift is far too big. Normally you would expect a shift between the DBR and the fundamental mode of about 2 to 3 nm. This indicates that the oxidation did not go perfectly. Probably the oxidation taper is oxidized all the way through and some of the AlGaAs layer(s) in the mirror form an aperture which confines the light in the cavity and is responsible for this reasonably high Q-factor.

Chapter 8

Conclusion/Outlook

8.1   Conclusion

With help of the side lobe reflection at 1064nm the oxidation can be monitored in real time. We can clearly see the oxidation front (blue region in Fig.7.1 move towards the center and this gives us an indication when to stop the oxidation. It is important to use the right temperature because otherwise there might be no contrast visible. At room temperature the best way to check the amount of confinement due to the oxidation taper is through reflection or photoluminescence measurements of the cavity modes. Both methods give a good contrast of the modes, although reflection goes much faster. For these techniques the mode splitting gives an indication of the size of the optical confinement due to oxidation taper at room temperature and also the quality factor can be determined. Due to absorption it was impossible to use these techniques beyond $150\,^{\circ}$C.

8.2   Outlook

Optimization of the process when monitoring the oxidation real time is needed especially in the reduction of the scan time. A faster scan will help to increase the accuracy regarding the time to stop the oxidation and can be reached by taking a smaller area to scan. This is especially important since the oxidation rate speeds up at the end of the process.
The theoretical model can be improved by adding temperature and absorption to the theoretical models in Fig.3.3. Especially the temperature dependence will have a big effect on the side lobes in the high wavelength range of the mirror as is shown in section 5.2. The influence of the absorption in that area is not so large.
It might also be worth trying to re-oxidize a sample; until now it is not clear why this is not possible. It seems that cleaning the sample before oxidizing with ammonium hydroxide is very crucial, because if this is not done then the oxidation might not start. Ammonium hydroxide will remove the oxide (probably not homogeneously), this way it might be possible to re-oxidize a sample which is very underoxidized. But removing the oxide will leave an empty space in the structure, which will have a lot of influence on the internal stress with as result that it is not possible to tune a quantum dot in resonance.

Another way of getting more control of the oxidation of the oxidation taper in the cavity is by putting a cover on some micropillars. This way you can only oxidize one row at the time and then you calibrate the setup to get a better aperture if you oxidize another row on the sample.

Chapter 9

Acknowledgements

Bibliography

[1] D. Leonard, M. Krishnamurthy, C. M. Reaves, S. P. Denbaars, and P. M. Petroff, "Direct formation of quantum-sized dots from uniform coherent islands of ingaas on gaas surfaces," *Appl. Phys. Lett*, vol. **63**, pp. 3203–3205, (1993).

[2] K. J. Vahala, "optical microcavities," *Nature*, vol. **424**, pp. 839–846, (2003).

[3] J. P. Reithmaier, A. Löffler, C. Hofmann, S. Kuhn, S. L. Reitzenstein, V. Keldysh, V. D. Kulakovskii, T. L. Reinecke, and A. Forchel, "Strong coupling in a single quantum dot-semiconductor microcavity system," *Nature*, vol. **432**, pp. 197–204, (2004).

[4] H. Lee, J. Johnson, M. He, J. Speck, and P. Petroff, "Strain engineered self-assembled semiconductor quantum dot lattices," *Appl. Phys. Lett.*, vol. **78**, pp. 105–107, (2001).

[5] T. D. Happ, I. I. Tartakovskii, V. D. Kulakovskii, J. Reithmaier, M. Kamp, and A. Forchel, "Enhanced light emission of ingaas quantum dots in a two-dimensional photonic-crystal defect microcavity," *Phys.Rev. B*, vol. **66**, p. 041303, (2002).

[6] A. Badolato, K. Hennessy, M. Atatüre, J. Dreiser, E. Hu, P. M. Petroff, and A. Imamoğlu, "Deterministic coupling of single quantum dots to single nanocavity modes," *Science*, vol. **308**, pp. 1158–1161, (2005).

[7] C. I. Ashby, M. M. Bridges, A. A. Allerman, and B. E. Hammons, "Origin of the time dependence of wet oxidation of algaas," *Applied Physics Letters*, vol. **75**, pp. 73–75, (1999).

[8] I. Marek Osiński Senior Member, T. Svimonishvili, G. A. Smolyakov, V. A. Smagley, P. Maćkowiak, and W. N. M. IEEE, "Temperature and thickness dependance of steam oxidation of alas in cylindrical mesa structures," *Photonics Technology Letters*, vol. **13**, pp. 687–689, (2001).

[9] P.-C. Ku and C. J.Chang-Hasnain, "Thermal oxidation of algaas: Modeling and process control," *IEEE journal of quantum electronics*, vol. **39**, pp. 577–585, (2003).

[10] G. Almuneau, R. Bossuyt, P. Collière, L. Bouscayrol, M. Condé, I. Suarez, V. Bardinal, and C. Fontaine, "Real-time in situ monitoring of wet thermal oxidation for precise confinement in vcsels," *Semiconductor science and technology*, vol. **225**, p. 105021, (2008).

[11] K. D. et al, "Advances in selective wet oxidation of algaas alloys," *Journal of selected topics in quantum electronics*, vol. **3**, pp. 916–926, (1997).

[12] J. Gudat, *Cavity Quantum Electrodynamics with Quantum Dots in Microcavities*. PhD thesis, University of Leiden, (2012).

[13] Hyochul, *Solid State Cavity QED systems: Designs and Applications*. PhD thesis, University of California Santa Barbara, (2009).

[14] B. thesis Keesjan de Vries, "Optical modes of micropillar cavities," (2009).

[15] H.Unlu, "A thermodynamic model for determining pressure and temperature effects on the bandgap energies and other properties of some semiconductors," *Solid State Electronics*, vol. **35**, pp. 1343–1352, (1992).

[16] Y.P.Varshni *Physica*, vol. **34**, pp. 149–155, (1967).

[17] "http://www.ioffe.ru/sva/nsm/semicond/index.html."

[18] "Vertical version 4.92, vertical structure design."

[19] R. Lemus, "Vibrational excitations in h_2o in the framework of a local model," *J. Mol. Spectrosc.*, vol. **225**, pp. 73–92, (2004).

[20] "http://www.lsbu.ac.uk/water/vibrat.html."